Mechanical properties of graphene oxide; A molecular dynamics study

Article *in* Fullerenes Nanotubes and Carbon Nanostructures · July 2016

DOI: 10.1080/1536383X.2016.1208180

CITATIONS
68

READS
4,290

2 authors:

Amir R. Khoei
Sharif University of Technology
249 PUBLICATIONS **5,972** CITATIONS
SEE PROFILE

Mohammad Sarkari Khorrami
Max Planck Institute for Iron Research GmbH
12 PUBLICATIONS **101** CITATIONS
SEE PROFILE

FULLERENES, NANOTUBES AND CARBON NANOSTRUCTURES
2016, VOL. 24, NO. 9, 594–603
http://dx.doi.org/10.1080/1536383X.2016.1208180

Taylor & Francis
Taylor & Francis Group

Mechanical properties of graphene oxide: A molecular dynamics study

A. R. Khoei and M. S. Khorrami

Department of Civil Engineering, Center of Excellence in Structures and Earthquake Engineering, Sharif University of Technology, Tehran, Iran

ABSTRACT

In this paper, the mechanical properties of graphene oxide are obtained using the molecular dynamics analysis, including the ultimate stress, Young modulus, shear modulus and elastic constants, and the results are compared with those of pristine graphene. It is observed that the increase of oxide agents (–O) and (–OH) leads to the increase of C–C bond length at each hexagonal lattice and as a result, alter the mechanical properties of the graphene sheet. It is shown that the elasticity modulus and ultimate tensile strength of graphene oxides (–O) and (–OH) decrease significantly causing the failure behavior of graphene sheet changes from the brittle to ductile. The results of shear loading tests illustrate that the increase of oxide agents (–O/–OH) results in the decrease of ultimate shear stress and shear module of the graphene sheet. It is shown that the increase of oxide agents in the graphene sheet leads to decrease of the elastic constants, in which the reduction of elastic properties in the armchair direction is more significant than the zigzag direction. Moreover, the graphene sheet with oxide agents (–O) and (–O/–OH) presents an anisotropic behavior.

ARTICLE HISTORY
Received 8 May 2016
Accepted 28 June 2016

KEYWORDS
Molecular dynamics; Graphene oxide; Mechanical properties; Anisotropic behavior

1. Introduction

Graphene is a two-dimensional lattice of carbon atoms that is constructed from a one-atom thick carbon layer. In the graphene, each carbon atom is bonded to three other carbon atoms, where their bonds are placed on one sheet and the angles between them are equal to 120°. In this case, carbon atoms are in a situation where a regular grid of hexagonal is ideally buildup. The C-C bond length of graphene is about 0.142 nm (1), and the thickness of graphene layer is about 0.341 nm (2,3).

The electrical, thermal, optical and mechanical properties of graphene are exceptional. Graphene is a perfect thermal conductor, the thermal conductivity of graphene was computed at the room temperature between $(4.84 \pm 0.44) \times 10^3$ and $(5.30 \pm 0.48) \times 10^3$ $\mathrm{w.m^{-1}k^{-1}}$ (4). The mechanical properties of graphene such as the ultimate tensile strength and ultimate strain were obtained by Zhao (5). Moreover, the mechanical properties of hydrogen-functionalized graphene were investigated by Kheirkhah et al. (6) and Pei et al. (7) and the graphene with atomic defect structure were studied by Wang et al. (8), Uberuaga et al. (9) and Mortazavi and Ahzi (10). It was reported that the nitrogen doping and other functionalized groups on graphene sheets can affect the mechanical properties of graphene (11). Furthermore, the chemical and physical properties of the graphene and graphene oxide were experimentally studied by Yadav et al. (12). Ansaria et al. (13) computed the Young modulus, failure strain and ultimate strength of monolayer graphene sheets with double vacancy defects; they also investigated vibrations of single layer graphene sheet with arbitrary edge conditions (14). On the basis of molecular dynamics analysis, the Young modulus, critical stress and critical strain of graphene were computed as 1.13 TPa, 180 GPa and 32.48%, respectively (15). The observed values achieved by the experimental investigation corresponding to the Young modulus, critical stress, and critical strain were reported as 1 TPa, 130 GPa and 25%, respectively (16). In addition, the Young modulus of graphene was calculated using the MM (17), CM (18), DFT (19), QM (20) and FEM (21) methods, as 1.39, 1.04, 1.05, 0.737 and 1.025 TPa, respectively.

Graphene oxide can be generally produced during the oxidation of graphite; while the pure graphene can be obtained by reducing the hydrazine (22). In 1859, graphine oxide was produced for the first time by a mixture of potassium chloride and nitric acid (23). Graphene oxide has many applications in industry; it has been used for removal of the radioactive material from water (24). Graphene oxide films can be produced by suspending the graphene oxide layers within the tank of hydrazine monohydrate to obtain the spongy sheets after about 10 hours of heating at 90°C. This structure is lightweight and porous, and possesses a high electrical conductivity. The reduced graphene oxide in a spongy shape has a better performance and more flexibility comparing to graphene oxide layers, as a material used in the organic absorbent. The performance of graphene oxide functionalized with various enzymes has been studied by researchers. The functionalized graphene oxide leads to an improvement in thermal stability and enzymes performance (24). These observations can be used both in industry and in the field of molecular biology. Moreover, the mechanical

CONTACT A. R. Khoei arkhoei@sharif.edu Department of Civil Engineering, Center of Excellence in Structures and Earthquake Engineering, Sharif University of Technology, P.O. Box. 11365-9313, Tehran, Iran.

Color versions of one or more of the figures in the article can be found online at www.tandfonline.com/lfnn.

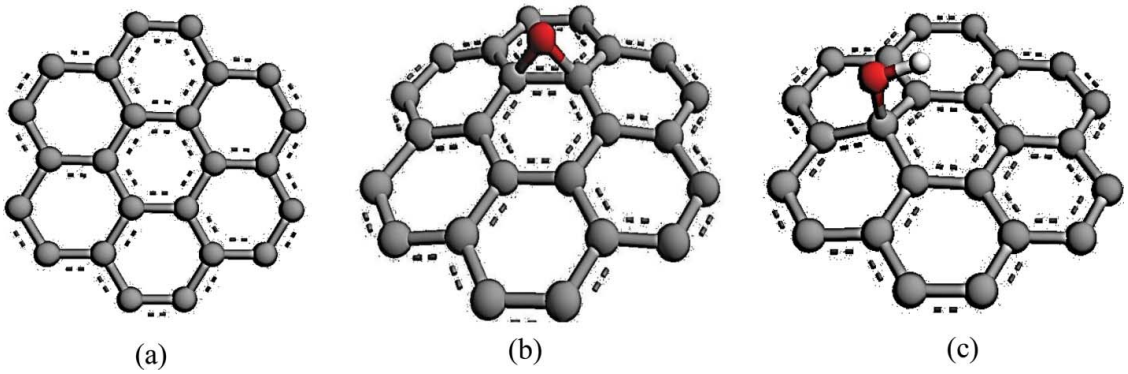

Figure 1. Schematically representation of the graphene sheet: (a) pristine graphene; (b) graphene with the oxide agent (–O) and (c) graphene with the oxide agent (–OH).

properties of graphene oxide films were obtained experimentally in laboratory by Forati et al. (25) and Kang et al. (26).

There are several research studies carried out in literature on the absorption of molecular oxygen on graphene and carbon nanotube; including the effect of chemical oxidation on the single-walled carbon nanotube (27), investigation of atomic, electronic and magnetic properties of gas sensor, electronic and spintronic devices due to adsorption of the molecular oxygen on doped graphene (28), mechanical properties of chiral carbon nanotubes under oxygen adsorption (29), the effect of oxygen adsorption and dissociation on graphene and nitrogen doped graphene for Li-air batteries (30), mechanical properties of oxygenated carbon nanotubes under physical adsorption of polymers (31), buckling behavior of single-walled carbon nanotubes under chemical adsorption of atomic oxygen and hydroxyl (32), the effect of oxygen adsorption and diffusion on single-layer graphene with topological defects (33), mechanical properties of graphene sheet under the absorption of molecular hydrogen physisorption (34) and mechanical properties of graphene sheet under fully covered hydrogen atoms functionalized on carbon atoms (35).

In this study, the mechanical properties of graphene oxide are obtained using the molecular dynamics analysis. The stress-strain curves of graphene and graphene oxide are presented together with the process of failure in the tensile and shear loadings. The critical stress, critical strain, Young modulus and shear modulus are computed for graphene and graphene oxide.

2. Molecular dynamics simulations

There are various techniques for computing the mechanical properties of nano-materials; including the molecular dynamics (MD), molecular mechanics (MM), continuum mechanics (CM), density functional theory (DFT), quantum mechanics (QM) and finite element method (FEM) (36–41). The molecular dynamics simulation is one of the most well-established techniques that can be used to predict the mechanical properties of graphene sheets based on an empirical potential. The molecular dynamics analysis is used to determine the equilibrium condition of graphene in tensile and shear experimental tests by minimizing the total potential energy with respect to the atomic positions. In this manner, the strain energy density together with the Virial stresses can be obtained from the molecular dynamics simulations, and as a consequence, the mechanical properties of graphene sheet can be attained from the continuum mechanics theory. In order to perform the molecular dynamics simulations, it is first necessary to obtain the initial coordinates of the atoms; for this purpose, the coordinate of graphene atoms is specified by the VMD software. In addition, the location of oxide agents (–O, –OH) on the graphene sheet are obtained using the quantum mechanics (QM) for a small model. In this manner, a general purpose quantum mechanical molecular model (AM1) (42) is employed to accurately determine the coordinates of atoms using the geometry optimization algorithm proposed in the Arguslab software. In the optimization process, the convergence is set to 1e–10 kcal/mol, and the line search algorithm of Broyden-Fletcher-Golfarb-Shanno (BFGS) is utilized. In Figure 1, a graphene sheet is presented together with the oxide agents (–O) and (–OH). The molecular dynamics simulations are performed using the LAMMPS software (Large-Scale Atomic/Molecular Massively Parallel Simulator) (43). The potential function between the atoms of graphene sheet is employed based on the optimized Tersoff model (44), which is similar to the original Tersoff potential (45,46). Moreover, the potential function for chemical bonds between the atoms of oxygen and graphene sheet (C–O) and also, the atoms of hydrogen and oxygen (O–H) is proposed based on the harmonic potential model. It must be noted that the energy evaluation on the basis of harmonic potential function is valid since the plane loading conditions, that is, the tensile and shear loading, are applied to the graphene sheet that do not affect the bond lengths of C–O and O–H considerably. Thus, the total potential energy of the system can then be written using the following equation as

$$E = \sum E_{\text{bond}} + \sum E_{\text{angle}} + \sum E_{\text{pair}} \tag{1}$$

in which E_{bond}, E_{angle} and E_{pair} are the harmonic potential, angle bending potential and pair potential between atoms, respectively. The harmonic potential E_{bond} is defined as

$$E_{\text{bond}} = K_{ij}\left(r_{ij} - r_0\right)^2 \tag{2}$$

where K_{ij} and r_{ij} are the bond stiffness and the distance between atom i and atom j, respectively, and r_0 denotes the equilibrium

distance. The angle bending potential E_{angle} is defined as

$$E_{\text{angle}} = K_{ijk}(\theta - \theta_0)^2. \tag{3}$$

where K_{ijk}, θ and θ_0 denote the constant force, the angle between atoms i, j and k, and the equilibrium angle, respectively. Finally, the pair potential between atoms E_{pair} is defined as

$$E_{\text{pair}} = E_{C-C} + E_{ij} \tag{4}$$

where the term E_{C-C} in the pair potential refers to the short-range interactions among carbon atoms, in which the potential function between the atoms of carbon is used based on the optimized Tersoff model. In the above relation, the term E_{ij} refers to the long-rang interaction among all types of atoms defined as

$$E_{ij} = \sum_{k\neq i}\sum_{l\neq i,j,k}\left\{4\varepsilon\left[\left(\frac{\sigma}{r_{ij}}\right)^{12} - \left(\frac{\sigma}{r_{ij}}\right)^{6}\right] + \frac{Cq_iq_j}{r_{ij}}\right\} \tag{5}$$

where ε, σ, C and q_i are the minimum energy, zero-potential distance, electrostatic distance and electron charge, respectively. The parameters of harmonic potential and angular bending for carbon, oxygen and hydrogen atoms are given in Table 1 (47,48).

In order to perform the tensile experimental test and obtain the mechanical properties of the bulk material, the periodic boundary conditions are employed in the both x- and y-directions using an appropriate strain rate. Moreover, to simulate the tensile and shear loading tests in the molecular dynamics simulations, the simulation box is continuously deformed using the "fix-deform" command in the LAMMPS program. The tensile test for graphene oxide (GO) is performed with the strain rate of 5e-4 1/ps. The time step for all numerical simulations is considered as 1e-3 ps. This time step was also utilized in simulations carried out by Ansari et al. (49) and Khoei et al. (50) that leads to an adequate accuracy. The size of the specimen is considered 5 nm for both horizontal and vertical directions. All numerical simulations are carried out at a constant temperature of 300 K employing the Nose-Hoover thermostat. In addition, the numerical integration for molecular dynamics analysis is performed based on the Velocity Verlet algorithm (51). Before applying the prescribed strain loading on the simulation box of samples, the specimens are relaxed under atomic internal forces to minimize the total potential energy of the system.

Table 1. Parameters of harmonic potential and angular bending for carbon, oxygen and hydrogen (28,29).

Parameters	Value
Harmonic bond stiffness K_{OC} (kcal/mol/Å^2)	334.3
Harmonic bond stiffness K_{OH} (kcal/mol/Å^2)	545
Equilibrium distance $r_{0_{OC}}$ (Å^2)	1.411
Equilibrium distance $r_{0_{OH}}$ (Å^2)	0.96
Harmonic angle stiffness K_{COH} (kcal/mol)	65
Equilibrium angle $\theta_{0_{OH}}$	108
Zero-potential distance σ_C (Å^2)	3.4
Zero-potential distance σ_O (Å^2)	3.15
Zero-potential distance σ_H (Å^2)	0.4
Minimum energy ε_C (kcal/mol)	0.07
Minimum energy ε_O (kcal/mol)	0.1521
Minimum energy ε_H (kcal/mol)	0.0460
Electrostatic constant C (Åkcal/mol)	332.1
Charge relative to the electron charge q_C (in pristine grapheme, sp2-hybridised)	0.0
Charge relative to the electron charge q_C (in triplet of COH, sp3- hybridized)	0.11
Charge relative to the electron charge q_C	0.54
Charge relative to the electron charge q_C	0.43

In molecular dynamics simulations, the strain energy density function can be used to evaluate the atomistic stresses as a measure of mechanical interactions. In this manner, the stress values can be obtained by differentiation from the strain energy density function with respect to the corresponding strain component, or directly from the atomic forces. Implementation of the strain energy density function requires variation of the strain component. One of the commonly used definitions for evaluation of the atomistic stress is the Virial stress; this stress is based on the generalization of the Virial theorem in thermodynamics which was originally used to calculate the system pressure. The Virial stress provides a unique concept to couple the deformation behavior of atomistic system with the continuum model. The Virial stress for the atom α can be defined as (52)

$$\sigma_{kl}^{\alpha} = \frac{1}{\Omega^{\alpha}}\left(-m^{\alpha}v_l^{\alpha}v_k^{\alpha} + \frac{1}{2}\sum_{\beta\neq\alpha} f_k^{\alpha\beta}r_l^{\alpha\beta}\right) \tag{6}$$

where Ω^{α} is the volume of atom α, m^{α} is the mass of atom α, $r_l^{\alpha\beta}$ is the distance between atoms α and β in the direction of l, and $f_k^{\alpha\beta}$ is the interactive force between atoms α and β in the direction of k. The summation over β covers all atoms in the neighborhood of atom α, and the indices k and l are the coordinate components of stress tensor. The thickness of the sample is considered as 3.4 Å, which is indeed the equilibrium distance between two graphene sheets. In molecular dynamics simulations, the volume of atom Ω^{α} is updated at each step to calculate the Virial stress components.

In order to determine the elastic constant properties of graphene and graphene oxide, the strain energy density is first derived by fitting a polynomial curve, and the elastic constant properties C_{ijkl} are then obtained for two-dimensional plane-stress problems as

$$C_{ijkl} = \frac{\partial^2 U}{\partial\varepsilon_{ij}\partial\varepsilon_{kl}} \tag{7}$$

where U is the strain energy density containing the total atomic potential energy and kinetic energy and, ε_{ij} and ε_{kl} denote the strain tensors. The relation between the stress and strain is defined as

$$\begin{Bmatrix}\sigma_{11}\\ \sigma_{22}\\ \sigma_{12}\end{Bmatrix} = \begin{bmatrix}C_{1111} & C_{1122} & 0\\ C_{1122} & C_{2222} & 0\\ 0 & 0 & C_{1212}\end{bmatrix}\begin{Bmatrix}\varepsilon_{11}\\ \varepsilon_{22}\\ \varepsilon_{12}\end{Bmatrix} \tag{8}$$

Considering the graphene oxide sheet in plane stress condition, the elastic modulus E_1 and E_2, the shear modulus G and the Poisson ratios υ_{12} and υ_{21} in the armchair and zigzag

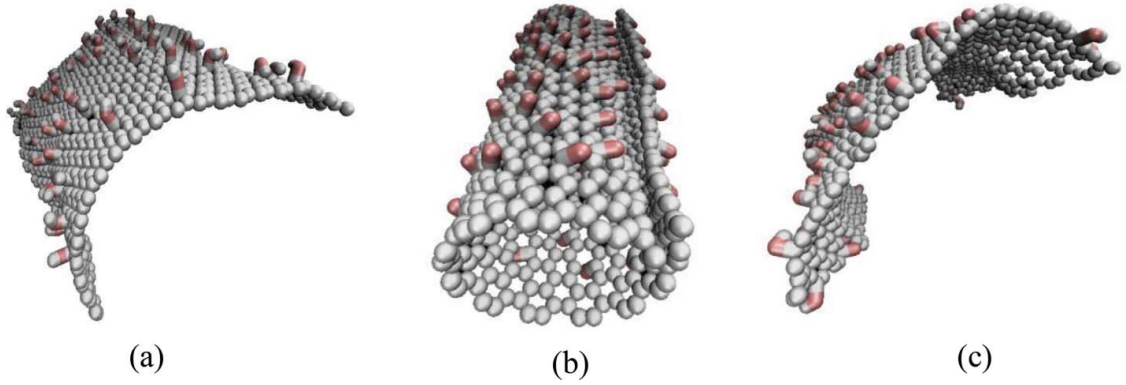

Figure 2. The configurations of graphene sheet with oxide agents (–O) and (–OH) on one side of the graphene sheet: (a) oxide agent (–OH); (b) oxide agent (–O) and (c) oxide agents (–O/–OH).

directions can be obtained as

$$E_1 = \frac{C_{1111}C_{2222} - {C_{1122}}^2}{C_{2222}}$$

$$E_2 = \frac{C_{1111}C_{2222} - {C_{1122}}^2}{C_{1111}} \quad G = \frac{C_{1212}}{2} \qquad (9)$$

$$\upsilon_{12} = \frac{C_{1122}}{C_{2222}}, \quad \upsilon_{21} = \frac{C_{1122}}{C_{1111}}$$

3. Results and discussion

In this section, the results of molecular dynamics simulations are presented for the graphene sheet at various percentages of oxide agents (–O), (–OH) and (–O/–OH). It must be noted that the oxide agents can be positioned on one side, or both sides of the graphene sheet. However, it has been observed here that if the oxide agents are placed only on one side of the graphene sheet it suffers from a severe curvature of the graphene sheet, as shown in Figure 2. Hence, the numerical simulations are performed with the oxide agents (–O), (–OH) and (–O/–OH) placed randomly on both sides of graphene sheet, as shown in Figure 3. Moreover, the periodic boundary conditions are employed in both directions to firstly model the graphene sheet in a plane condition, and secondly determine the mechanical properties of the graphene in the case of bulk material. In Figure 4, the atomistic configuration of the molecular dynamics analysis is presented for the graphene sheet functionalized by agents (–O), (–OH) and (–O/–OH), in which the uniaxial tension is applied in both the zigzag and armchair directions. Before each simulation, the graphene sheet is relaxed to acquire the equilibrium condition at zero strain. A uniaxial tension is then applied in both directions, independently. In order to investigate the stability of the MD analysis, the graphene sheet with 20% of oxide agents (–O) and (–OH) is relaxed for a time period of 50 ps, as shown in Figure 5. Obviously, the total energy becomes constant after 5 ps. Note that the occurrence of fluctuation in the curves of total energy is due to the MD analysis performed at the room temperature of 300 K.

In Figure 6, the stress-strain curves are plotted under the uniaxial tension in zigzag and armchair directions for the

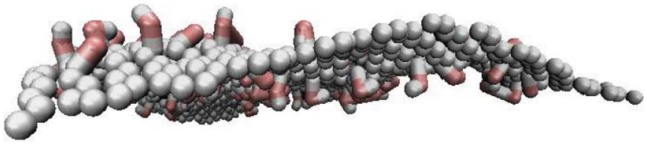

Figure 3. The configurations of graphene sheet with oxide agents (–O) and (–OH) on two sides of the graphene sheet.

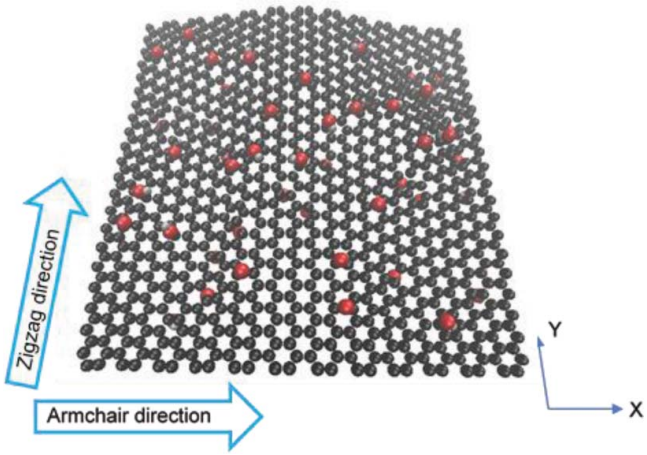

Figure 4. Representation of a graphene sheet with the oxide agents (–O) and (–OH) in armchair and zigzag directions.

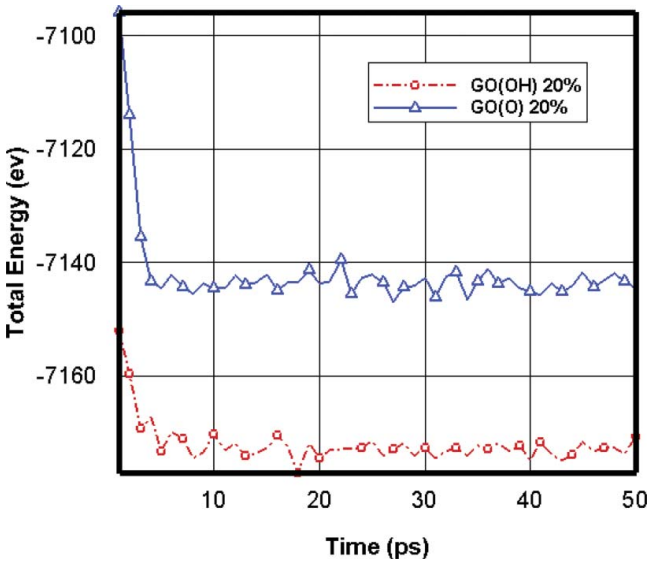

Figure 5. Evolutions of the total energy for a graphene sheet with oxide agents (–O) and (–OH) during the relaxation phase.

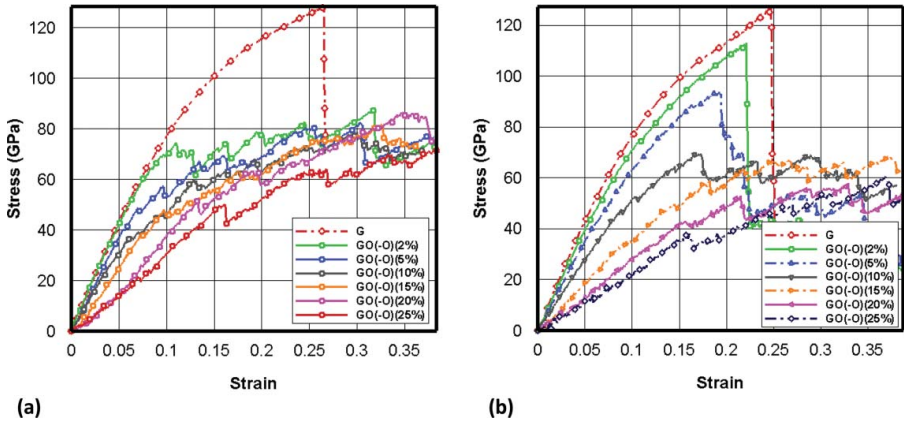

Figure 6. The stress–strain curves for the graphene sheet at various percentages of oxide agent (–O) under tensile loading: (a) zigzag direction and (b) armchair direction.

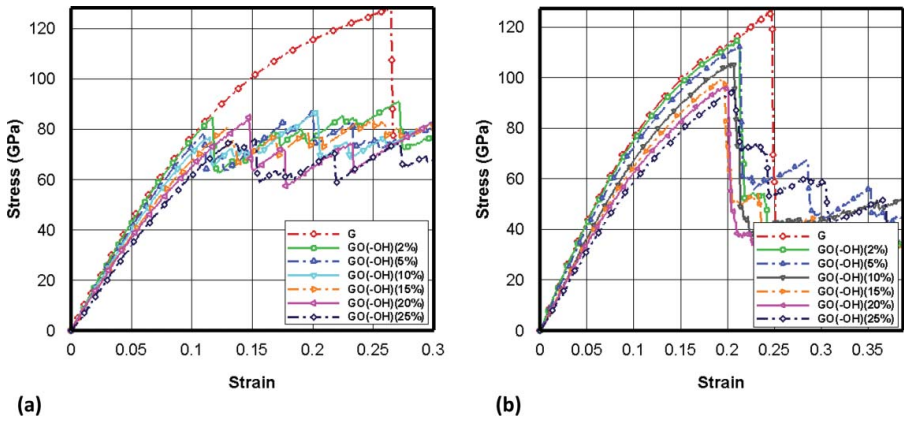

Figure 7. The stress–strain curves for the graphene sheet at various percentages of oxide agent (–OH) under tensile loading: (a) zigzag direction and (b) armchair direction.

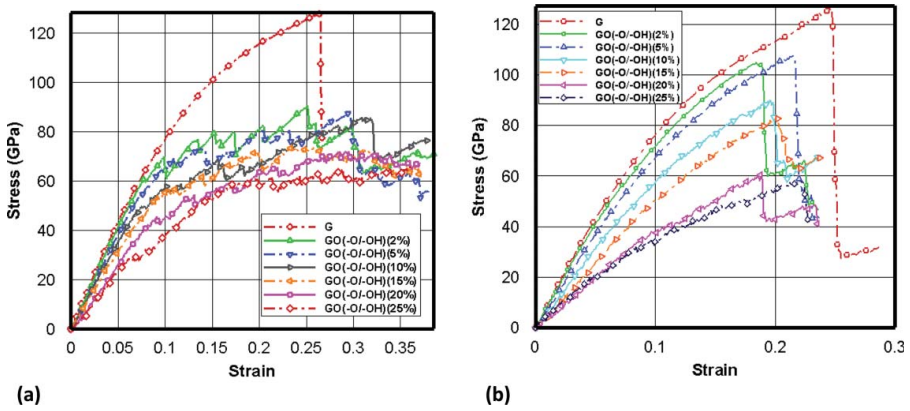

Figure 8. The stress–strain curves for the graphene sheet at various percentages of oxide agents (–O/–OH) under tensile loading: (a) zigzag direction and (b) armchair direction.

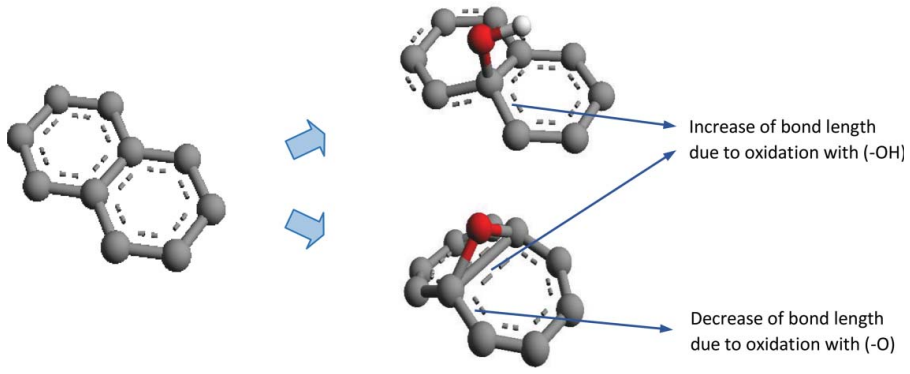

Figure 9. The hexagonal lattice of graphene sheet after oxidation with agents (–O) and (–OH).

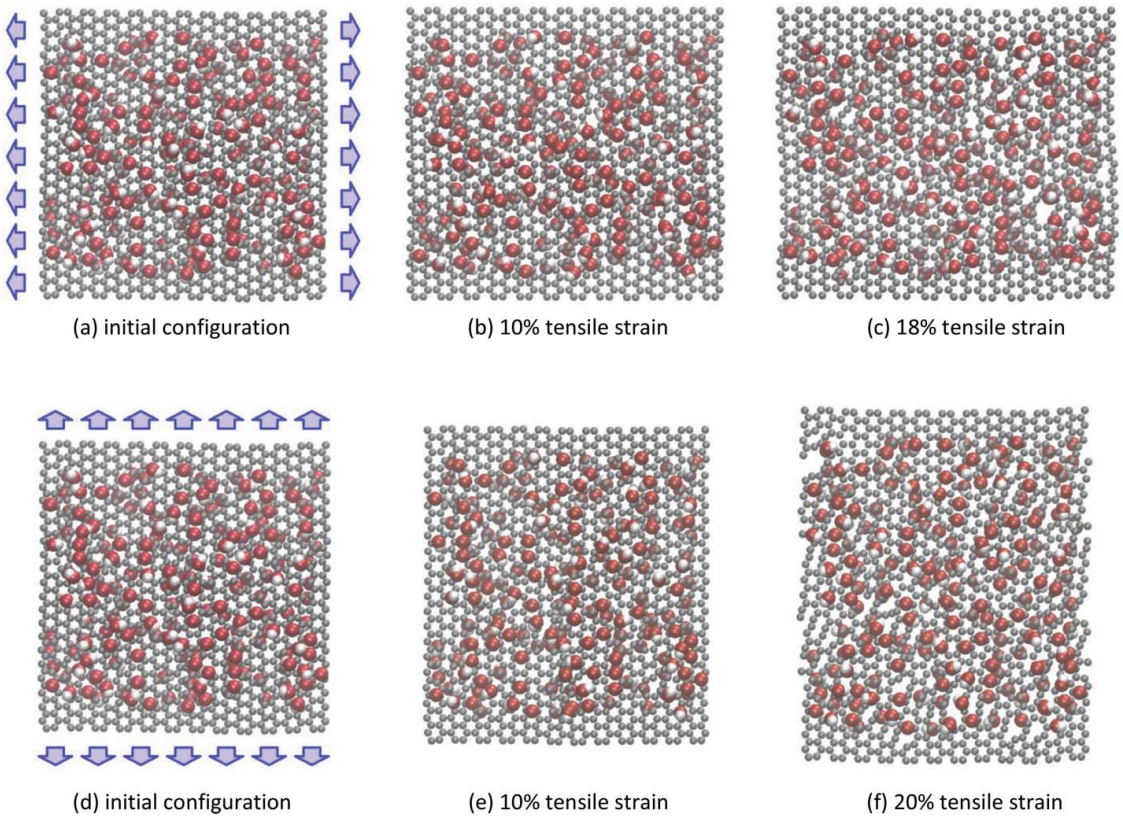

Figure 10. The graphene sheet with 20% oxide agents (–O/–OH) under tensile loading: (a–c) tensile in armchair direction and (d–f) tensile in zigzag direction.

graphene sheet at various oxide agents (–O). In all numerical simulations, the oxide agents (–O) are located randomly on both sides of the graphene sheet, and the boundary conditions are employed periodically in both directions of the graphene sheet. Obviously, by increasing the oxide agent (–O), the slope of stress-strain curve as well as the ultimate tensile stress reduce. The reason can be related to the C–C bond length at each hexagonal lattice of the graphene sheet connected to an oxide agent (–O). In fact, the oxide agent (–O) results in the increase of C–C bond length at those hexagonal lattices connected to an oxide agent (–O) that leads to a reduction of the ultimate tensile strength in the graphene sheet. In Figure 7, the tensile stress-strain curves are plotted in zigzag and armchair directions for the graphene sheet at various oxide agents (–OH). According to this figure, it can be revealed that the increase of oxide agent (–OH) leads to a decrease in the ultimate tensile strength. It is important to point out once again that the bond between the oxide agent (–OH) and a hexagonal lattice of the graphene sheet leads to an increase of the C–C

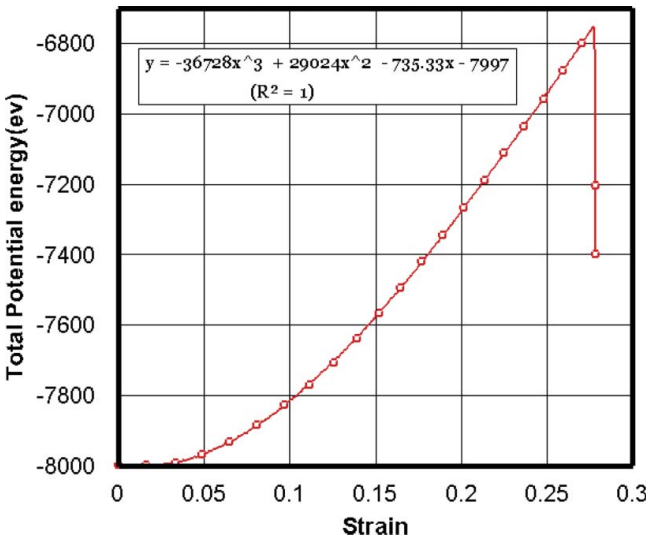

Figure 11. The evolution of total potential energy in the tensile test for a pristine graphene sheet.

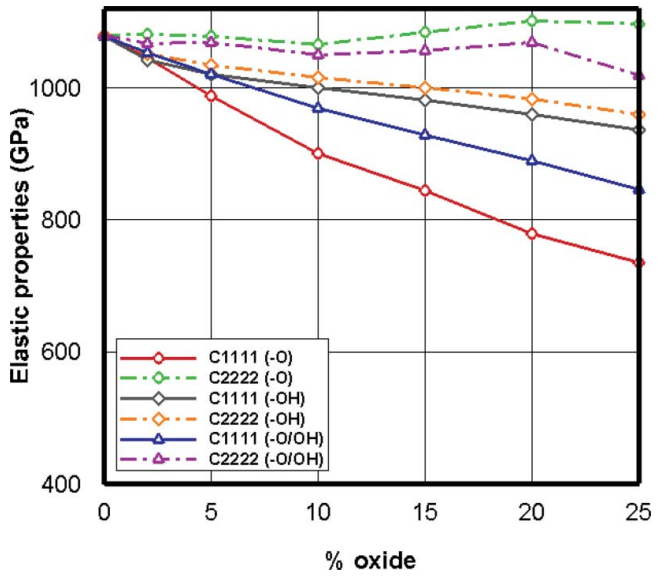

Figure 12. The evolutions of elastic constant C_{1111} (armchair direction) and C_{2222} (zigzag direction) for the graphene sheet with oxide agents (–O), (–OH) and (–O/–OH).

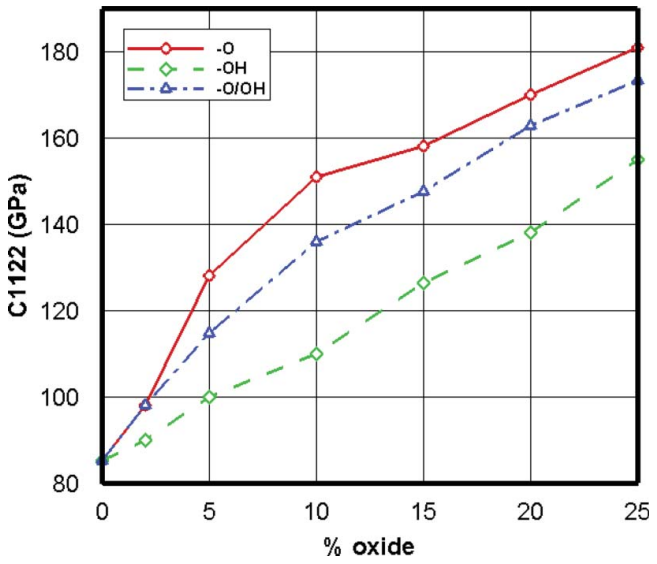

Figure 13. The evolutions of elastic constant C_{1122} for the graphene sheet with oxide agents (–O), (–OH) and (–O/–OH).

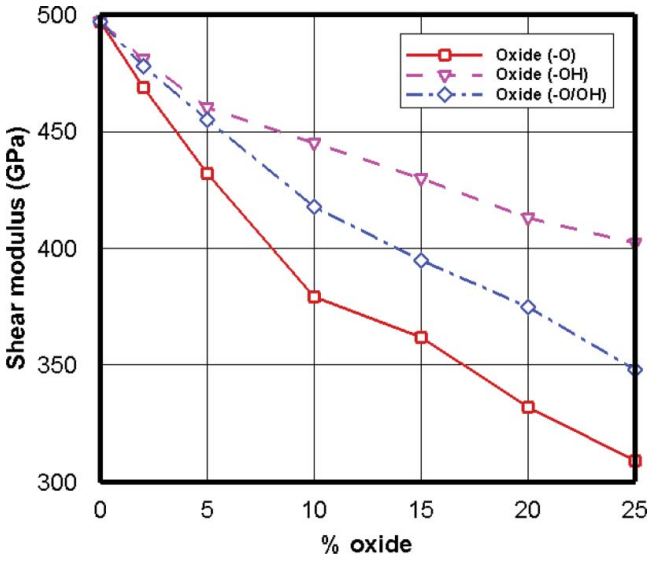

Figure 15. The evolutions of shear modulus G for the graphene sheet with oxide agents (–O), (–OH) and (–O/–OH).

bond length. A comparison between Figures 6 and 7 provides an evidence of more influence of the oxide agent (–O) on the strength of graphene sheet compared to the oxide agent (–OH).

In order to investigate the mechanical properties of graphene sheet with oxide agents (–O/–OH), the atoms of (–O) and (–OH) are placed randomly on each side of the graphene sheet. In Figure 8, the stress–strain curves of graphene sheet are plotted at various percentages of oxide agents (–O/–OH) in the zigzag and armchair directions. Obviously, by increasing the oxide agents (–O/–OH), the ultimate tensile strength decreases and the elasticity modulus of graphene sheet reduces significantly; in fact, the results are similar to those obtained for the graphene sheet at various oxide agents (–O), as given in Figure 6. Furthermore, it has been observed that the increase of oxide agents (–O/–OH) transforms the failure behavior of the graphene sheet from the brittle to ductile. It can be highlighted from Figures 6–8 that the decrease of ultimate strength in the zigzag direction is more significant than its reduction in the armchair direction. Moreover, the graphene oxide experiences the brittle failure in armchair direction since the C–C bond length between the atoms of each hexagonal lattice increases. As it can be seen from Figure 9, the C–C bond length increases in all directions of the hexagonal lattice when the oxide agent (–OH) is utilized. However, the oxide agent (–O) increases the C–C bond length only in one direction, while the C–C bond length reduces in other directions. In Figure 10, the deformed configurations of graphene sheet with 20% oxide agents (–O/–OH) are presented at different tensile loadings in the armchair and zigzag directions.

In order to determine the elastic properties of the graphene sheet functionalized by various percentages of oxide agents (–O), (–OH) and (–O/–OH), the strain energy density function is derived for each case by fitting a polynomial curve to

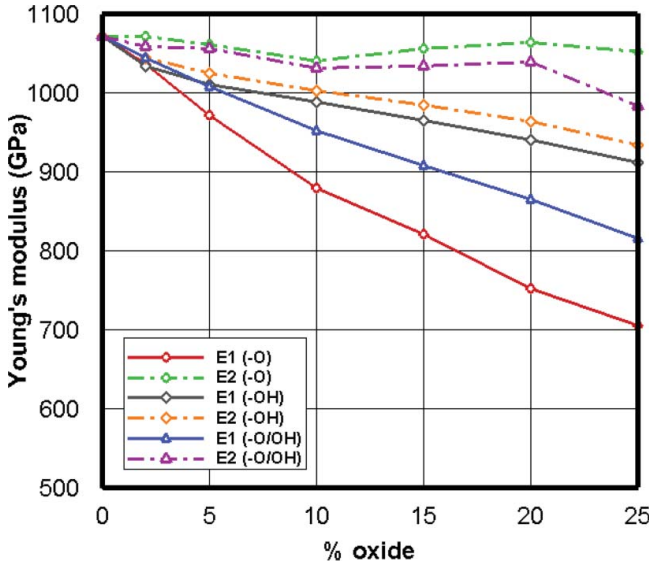

Figure 14. The evolutions of elastic modulus E_1 in armchair direction and E_2 in zigzag direction for the graphene sheet with oxide agents (–O), (–OH) and (–O/–OH).

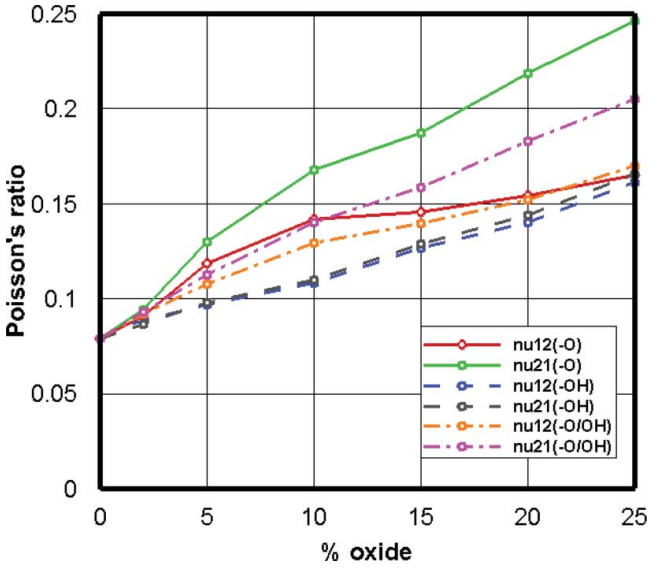

Figure 16. The evolutions of Poisson ratios υ_{12} and υ_{21} in the armchair and zigzag directions for the graphene sheet with oxide agents (–O), (–OH) and (–O/–OH).

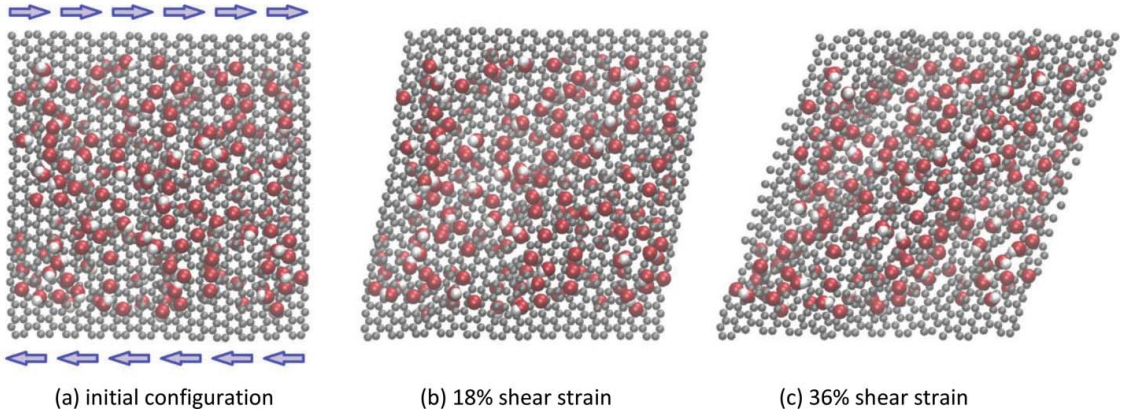

Figure 17. The graphene sheet with 20% oxide agents (–O/–OH) under shear loading in armchair direction.

numerical data. In Figure 11, the evolution of total potential energy is presented as a function of the strain for a pristine graphene sheet under uniaxial tension in the armchair direction. Obviously, the potential energy increases as the strain increases until it reaches a critical point where a sudden drop of the energy occurs. The elastic constants C_{1111}, C_{2222}, C_{1122} and C_{1212} can be obtained according to relation (8) by taking the second derivatives of the strain energy density function with respect to the corresponding strain component. For example for the pristine graphene sheet of 50 × 50 × 3.4 Å under uniaxial tension, the strain energy function is extracted from Figure 11 as follows; $U = -36728\ \varepsilon_{11}^3 + 29024\ \varepsilon_{11}^2 - 735\ \varepsilon_{11} - 7997$ (ev), in which the first elastic constant is computed by $C_{1111} = \frac{\partial^2 U}{\partial \varepsilon_{11} \partial \varepsilon_{11}} = 1092$ GPa.

Alternatively, the other elastic constants C_{2222}, C_{1122} and C_{1212} can be obtained by taking the second derivatives of the energy function U with respect to the strain components as $\frac{\partial^2 U}{\partial \varepsilon_{22} \partial \varepsilon_{22}}$, $\frac{\partial^2 U}{\partial \varepsilon_{11} \partial \varepsilon_{22}}$ and $\frac{\partial^2 U}{\partial \varepsilon_{12} \partial \varepsilon_{12}}$, respectively. The procedure can then be followed by evolutions of the elastic constants at various percentages of oxide agents (–O), (–OH) and (–O/–OH). In Figure 12, the evolutions of elastic constants C_{1111} and C_{2222} are plotted corresponding to the armchair and zigzag directions for the graphene sheet with oxide agents (–O), (–OH) and (–O/–OH). Obviously, the increase of oxide agents in the graphene leads to the decrease of elastic constants C_{1111} and C_{2222}, in which the reduction of elastic properties in the armchair direction is more significant than the zigzag direction. Moreover, the oxide agent (–O) has an influence on the reduction of elastic constant C_{1111}, while the oxide agent (–OH) makes an important effect on the reduction of elastic constant C_{2222}. In Figure 13, the evolutions of elastic constant C_{1122} are plotted for the graphene sheet with oxide agents (–O), (–OH) and (–O/–OH). Clearly, the increase of oxide agent leads to increase of the elastic constant C_{1122}. In Figure 14, the evolutions of elastic modulus E_1 in armchair direction and E_2 in zigzag direction are plotted for the graphene sheet with oxide agents (–O), (–OH) and (–O/–OH). It is interesting to highlight that the pristine graphene has an isotropic behavior with similar elastic properties in armchair and zigzag directions; however, the graphene sheet with oxide agents (–O) and (–O/–OH) has anisotropic behavior with different properties at two directions. Moreover, the increase of oxide agent (–O) in the graphene sheet results in a large difference of elastic property between the Young modulus of E_1 and E_2, where a highly anisotropic behavior can be observed for the graphene sheet with 25% oxide (–O). It must be noted that there is almost similar elastic property between the Young modulus of E_1 and E_2 for the graphene with oxide agent (–OH), in which an isotropic behavior can be seen from this figure. According to the experimental data reported by Kang et al. (26), the Young modulus of graphene sheet with 25% of oxide agents (–O/–OH) is about 700 GPa in the armchair direction, which is numerically obtained here as about 800 GPa.

In Figure 15, the evolutions of shear modulus G are plotted for the graphene sheet with oxide agents (–O), (–OH) and (–O/–OH). Obviously, the shear modulus G decreases as the percentage of oxide increases in the graphene sheet, where a great reduction of the shear modulus can be observed in the case of oxide agent (–O). In Figure 16, the evolutions of Poisson ratios υ_{12} and υ_{21} are plotted in the armchair and zigzag directions for the graphene sheet with oxide agents (–O), (–OH) and (–O/–OH). Clearly as discussed earlier, the pristine graphene has an isotropic behavior with similar Poisson ratio in

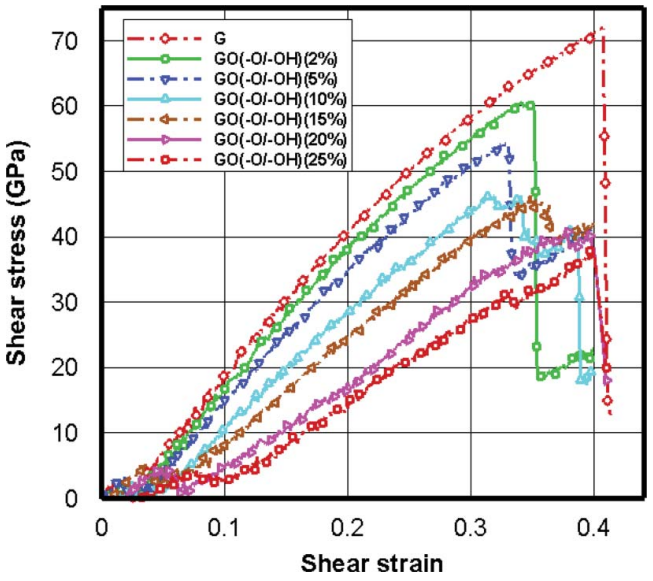

Figure 18. The shear stress–shear strain curves for the graphene sheet at various percentages of oxide agents (–O/–OH) under shear loading in armchair direction.

armchair and zigzag directions; the graphene sheet with oxide agent (–OH) has an isotropic behavior; and the graphene sheets with oxide agents (–O) and (–O/–OH) behave anisotropic with a highly anisotropic behavior in the case of oxide agent (–O). Finally, the results of shear loading tests are presented in Figures 17 and 18 for the graphene sheet at various percentages of oxide agents (–O/–OH). In Figure 17, the deformed configurations of graphene sheet with 20% oxide agents (–O/–OH) are presented at different shear loadings in armchair direction. In Figure 18, the shear stress–shear strain curves of the graphene sheet are plotted at various percentages of oxide agents (–O/–OH) in armchair direction. Obviously, the increase of oxide agents (–O/–OH) leads to the decrease of ultimate shear stress as well as the shear modulus of the graphene sheet.

4. Conclusions

In the present paper, the mechanical properties of the graphene oxide were obtained at various percentages of (–O), (–OH) and (–O/–OH) under tensile and shear loadings using molecular dynamics simulations. The stress-strain curves of the pristine graphene as well as the graphene oxides (–O), (–OH) and (–O/–OH) were presented and the values of ultimate stress and strain, Young modulus, shear modulus and Poisson ratio were computed for the pristine graphene and graphene oxides in the armchair and zigzag directions. It was shown that the increase of oxide agents leads to reduction of the Young modulus as well as the ultimate tensile stress in the graphene sheet, in which the influence of oxide agent (–O) is more significant on the strength of graphene sheet. In fact, the increase of oxide agents causes the increase of C–C bond length at each hexagonal lattice of the graphene sheet connected to an oxide agent, which results in the increase of C-C bond length and as a consequence the reduction of ultimate tensile strength. Moreover, it was observed that the increase of oxide agents (–O/–OH) transforms the failure behavior of the graphene sheet from brittle to ductile. It was shown that the increase of oxide agents in the graphene sheet leads to decrease of the elastic constants, in which the reduction of elastic properties in the armchair direction is more significant than the zigzag direction. Furthermore, the oxide agent (–O) has a significant influence on the reduction of elastic constant C_{1111}, and the oxide agent (–OH) on the reduction of elastic constant C_{2222}. It was demonstrated that the pristine graphene as well as the graphene sheet with oxide agent (–OH) have the isotropic behavior with similar elasticity modulus and Poisson ratio in armchair and zigzag directions; however, the graphene sheets with oxide agents (–O) and (–O/–OH) behave anisotropic with the highly anisotropic behavior in the case of oxide agent (–O).

References

1. Delhaes, P. (2001) *Graphite and Precursors*, CRC Press.
2. Huang, Y., Wu, J., and Hwang, K. C. (2006) Thickness of graphene and single-wall carbon nanotubes. *Phys. Rev. B*, 74: 245413.
3. Namilae, S., Chandra, N., and Shet, C. (2004) Mechanical behavior of functionalized nanotubes. *Chem. Phys. Lett.*, 387: 247–252.
4. Chen, S., Wu, Q., Mishra, C., Kang, J., Zhang, H., Cho, K., Cai, W., Balandin, A. A., and Ruoff, R. S. (2012) Thermal conductivity of isotopically modified graphene. *Nature Mater.*, 11: 203–207.
5. Zhao, N. H. (2010) Temperature and strain-rate dependent fracture strength of graphene. *J. Appl. Phys.*, 108: 064321.
6. Kheirkhah, A. H., Iranizad, E. S., Raeisi, M., and Rajabpour, A. (2014) Mechanical properties of hydrogen functionalized graphene under shear deformation: A molecular dynamics study. *Solid State Comm.*, 177: 98–102.
7. Pei, Q. X., Zhang, Y. W., and Shenoy, V. B. (2010) A molecular dynamics study of the mechanical properties of hydrogen functionalized graphene. *Carbon*, 48: 898–904.
8. Wang, M. C., Yan, C., Ma, L., Hu, N., and Chen, M. W. (2012) Effect of defects on fracture strength of graphene sheets. *Comput. Mater. Sci.*, 54: 236–239.
9. Uberuaga, B. P., Stuart, S. J., Windl, W., Masquelier, M. P., and Voter, A. F. (2012) Fullerene and graphene formation from carbon nanotube fragments. *Comput. Theo. Chem.*, 987: 115–121.
10. Mortazavi, B., and Ahzi, S. (2013) Thermal conductivity and tensile response of defective graphene: A molecular dynamics study. *Carbon*, 63: 460–470.
11. Denis, P. A., Huelmo, C. P., and Iribarne, F. (2014) Theoretical characterization of sulfur and nitrogen dual-doped graphene. *Comput. Theo. Chem.*, 1049: 13–19.
12. Yadav, M., Rhee, K. Y., and Park, S. J. (2014) Synthesis and characterization of graphene oxide/ carboxy-methylcellulose/alginate composite blend films. *Carbohydr. Polym.*, 110: 18–25.
13. Ansari, R., Motevalli, B., Montazeri, A., and Ajori, S. (2011) Fracture analysis of monolayer graphene sheets with double vacancy defects via MD simulation. *Solid State Comm.*, 151: 1141–1146.
14. Ansari, R., Shahabodini, A., and Rouhi H. (2015) A nonlocal plate model incorporating interatomic potentials for vibrations of graphene with arbitrary edge conditions. *Curr. Appl. Phys.*, 15: 1062–1069.
15. Ni, Z., Bu, H., Zou, M., Yi, H., Bi, K., and Chen, Y. (2010) Anisotropic mechanical properties of graphene sheets from molecular dynamics. *Phys. B: Cond. Matter*, 405: 1301–1306.
16. Lee, C., Wei, X., Kysar, J. W., and Hone, J. (2008) Measurement of the elastic properties and intrinsic strength of monolayer graphene. *Science*, 321: 385–388.
17. Kvashnin, A. G., Sorokin, P. B., and Kvashnin, D. G. (2010) The theoretical study of mechanical properties of graphene membranes. *Fuller. Nanotub. Carbon Nanostruct.*, 18: 497–500.
18. Shokrieh, M. M., and Rafiee, R. (2010) Prediction of Young's modulus of graphene sheets and carbon nanotubes using nanoscale continuum mechanics approach. *Mater. Des.*, 31: 790–795.
19. Liu, F., Ming, P., and Li, J. (2007) Ab initio calculation of ideal strength and phonon instability of graphene under tension. *Phys. Rev. B*, 76: 064120.
20. Yanovsky, Y. G., Nikitina, E. A., Karnet, Y. N., and Nikitin, S. M. (2009) Quantum mechanics study of the mechanism of deformation and fracture of graphene. *Phys. Mesomech.*, 12: 254–262.
21. Sakhaeepour, A. (2009) Elastic properties of single-layered graphene sheet. *Solid State Comm.*, 149: 91–95.
22. Singh, V., Joung, D., Zhai, L., Das, S., Khondaker, S. I., and Seal, S. (2011) Graphene based materials: Past, present and future. *Prog. Mater. Sci.*, 56: 1178–1271.
23. Brodie, B. C. (1859) On the atomic weight of graphite. *Philos. Trans. Royal Soc. London*, 149: 249–259.
24. Romanchuk, A. Y., Slesarev, A. S., Kalmykov, S. N., Kosynkin, D. V., and Tour, J. M. (2013) Graphene oxide for effective radionuclide remova. *Phys. Chem. Chem. Phys.*, 15: 2321–2327.
25. Forati, T., Atai, M., Rashidi, A. M., Imani, M., and Behnamghader, A. (2013) Physical and mechanical properties of graphene oxide/polyethersulfone nanocomposites. *Polym. Adv. Tech.*, 25: 322–328.
26. Kang, S. H., Fang, T. H., Hong, Z. H., and Chuang, C. H. (2013) Mechanical properties of free-standing graphene oxide. *Diamond Relat. Mater.*, 38: 73–38.
27. Zhang, J., Zou, H., Qing, Q., Yang, Y., Li, Q., Liu, Z., Guo, X., and Du, Z. (2003) Effect of chemical oxidation on the structure of single-walled carbon nanotubes. *J. Phys. Chem. B*, 107: 3712–3718.
28. Dai, J., and Yuan, J. (2010) Adsorption of molecular oxygen on doped graphene: Atomic, electronic, and magnetic properties. *Phys. Rev. B*, 81: 165414.

29. Ansari, R., Mirnezhad, M., and Sadeghi, F. (2015) Elastic properties of chiral carbon nanotubes under oxygen adsorption. *Physica E: Low-dim. Sys. Nanostruct.*, 70: 129–134.
30. Yan, H. J., Xu, B., Shi, S. Q., and Ouyang, C. Y. (2012) First-principles study of the oxygen adsorption and dissociation on graphene and nitrogen doped graphene for Li-air batteries. *J. Appl. Phys.*, 112: 104316.
31. Ansari, R., Ajori, S., and Rouhi, S. (2015) Structural and elastic properties and stability characteristics of oxygenated carbon nanotubes under physical adsorption of polymers. *Appl. Surface Sci.*, 332: 640–647.
32. Ansari, R., Ajori, S., and Ameri, A. (2014) Elastic and structural properties and buckling behavior of single-walled carbon nanotubes under chemical adsorption of atomic oxygen and hydroxyl. *Chem. Phys. Lett.*, 616: 120–125.
33. Mehmood, F., Pachter, R., Lu, W., and Boeckl, J. J. (2013) Adsorption and diffusion of oxygen on single-layer graphene with topological defects. *J. Phys. Chem. C*, 117: 10366–10374.
34. Mirnezhad, M., Ansari, R., Seifi, M., Rouhi, H., and Faghihnasiri, M. (2012) Mechanical properties of graphene under molecular hydrogen physisorption: An ab initio study. *Solid State Comm.*, 152: 842–845.
35. Ansari, R., Mirnezhad, M., and Rouhi, H. (2015) Mechanical properties of fully hydrogenated graphene sheets. *Solid State Comm.*, 201: 1–4.
36. Lu, G., Tadmor, E. B., and Kaxiras, E. (2006) From electrons to finite elements: A concurrent multi-scale approach. *Phys. Rev. B*, 73: 024108.
37. Khoei, A. R., and Ghahremani, P. (2012) Temperature-dependent multi-scale modeling of surface effects in nano-materials. *Mech. Mat.*, 46: 94–112.
38. Khoei, A. R., DorMohammadi, H., and Aramoon, A. (2013) Multi-scale modeling of edge effect on band gap offset in polygonal cross-section Si nanowires. *Comput. Mat. Sci.*, 79: 262–275.
39. Yang, Q., Biyikli, E., and To, A. C. (2013) Multiresolution molecular mechanics: Statics. *Comp. Meth. Appl. Mech. Eng.*, 258: 26–38.
40. Khoei, A. R., Ghahremani, P., and DorMohammadi, H. (2014) Multi-scale modeling of surface effects in nano-materials with temperature-related Cauchy-Born hypothesis via the modified boundary Cauchy-Born model. *Int. J. Numer. Meth. Eng.*, 97: 79–110.
41. Khoei, A. R., Jahanbakhshi, F., and Aramoon, A. (2015) A concurrent multi-scale technique in modeling heterogeneous FCC nano–crystalline structures. *Mech. Mat.*, 83: 40–65.
42. Dewar, M. J. S., Zoebisch, E. G., Healy, E. F., and Stewart, J. J. P. (1985) Development and use of quantum mechanical molecular models. 76. AM1: a new general purpose quantum mechanical molecular model. *J. Am. Chem. Soc.*, 107: 3902–3909.
43. Plimpton, S. (1995) Fast parallel algorithms for short-range molecular dynamics. *J. Comp. Phys.*, 117: 1–19.
44. Lindsay, L., and Broido D. (2010) Erratum: Optimized Tersoff and Brenner empirical potential parameters for lattice dynamics and phonon thermal transport in carbon nanotubes and graphene. *Phys. Rev. B*, 81: 205441.
45. Tersoff, J. (1988) New empirical approach for the structure and energy of covalent systems. *Phys. Rev. B*, 37: 6991.
46. Tersoff, J. (1988) Empirical interatomic potential for carbon, with applications to amorphous carbon. *Phys. Rev. Lett.*, 61: 2879–2882.
47. Stuart, S. J., Tutein, A. B., and Harrison J. A. (2000) A reactive potential for hydrocarbons with intermolecular intractions. *J. Chem. Phys.*, 112: 6472–6486.
48. MacKerell, A. D., Bashford, J. D., Bellott, M., Dunbrack, R. L., and Evanseck, J. J. D. (1998) All-atom empirical potential for molecular modeling and dynamics studies of proteins. *J. Phys. Chem. B*, 102: 3586–3616.
49. Ansari, R., Ajori, S., and Motevalli, B. (2012) Mechanical properties of defective single-layered graphene sheets via molecular dynamics simulation. *Superlatt. Microstruct.*, 51: 274–289.
50. Khoei, A. R., Ban, E., Banihashemi, P., and Qomi, M. J. A. (2011) Effects of temperature and torsion speed on torsional properties of single-walled carbon nanotubes. *Mater. Sci. Eng. C*, 31: 452–457.
51. Griebel, M., Knapek, S., and Zumbusch, G. (2007) *Numerical Simulation in Molecular Dynamics Numerics, Algorithms, Parallelization, Applications*, Springer.
52. Tsai, D. H. (1979) The virial theorem and stress calculation in molecular dynamics. *J. Chem. Phys.*, 70: 1375–1382.